J. Fluid Mech. (2009), *vol.* 637, *pp.* 241–265. © Cambridge University Press 2009
doi:10.1017/S0022112009990656

The effects of hindered mobility and depletion of particles in near-wall shear flows and the implications for nanovelocimetry

PETER HUANG†, JEFFREY S. GUASTO‡
AND KENNETH S. BREUER

Division of Engineering, Brown University, Providence, RI 02915, USA

(Received 20 October 2008; revised 21 May 2009; accepted 30 May 2009; first published online 17 September 2009)

The behaviour of spherical Brownian particles in a near-wall shear flow is explored using Langevin simulations and experimental measurements, focusing on the effects of anisotropic hindered particle mobility and the formation of a particle depletion layer due to repulsive forces. The results are discussed in the context of particle velocity distributions obtained by near-wall image-based velocimetry. It is observed that the shear force and dispersion dominate at high Péclet number ($Pe > 3$), and the asymmetric shapes of particle velocity distributions are attributed to broken symmetry due to the presence of the wall. Furthermore, the excursions outside the observation depth between image acquisitions and the shear-induced slowdowns of tracer particles cause significant measurement bias for long and short inter-frame time intervals, respectively. Also impeding the measurement accuracy is the existence of a near-wall particle depletion layer that leads to an overestimation of the fluid velocity. An analytical protocol to infer the correct fluid velocity from biased measurements is presented.

1. Introduction

Colloidal particle-based image velocimetry is a widely utilized experimental technique for measuring fluid velocity profiles and other physical quantities. Its accuracy heavily relies on the assumption that tracer particles will conform to local fluid translational motion. In the past decade, particle image velocimetry (PIV) has been extended to the micro- (Santiago *et al.* 1998) and nanoscale (Zettner & Yoda 2003; Jin *et al.* 2004; Guasto, Huang & Breuer 2006; Huang, Guasto & Breuer 2006; Bouzigues, Tabeling & Bocquet 2008; Guasto & Breuer 2008; Li & Yoda 2008; Pouya *et al.* 2008) where the typical size of tracer particles has also decreased from microns to nanometres. At these physical length scales, Brownian motion of tracer particles can be quite significant, thus violating the assumption that tracer particles travel at velocities equal to that of the surrounding fluid. Consequently, conducting an accurate velocimetry experiment requires a good understanding and a careful treatment of Brownian motion via either a thorough error analysis (Santiago *et al.* 1998), an ensemble correlation averaging technique (Wereley & Meinhart 2005), a

---

† Present address: Department of Mechanical Engineering, Binghamton University, Binghamton, NY 13902, USA. Email address for correspondence: phuang@binghamton.edu

‡ Present address: Department of Physics, Haverford College, Haverford, PA 19041, USA.

statistical analysis of the particle ensemble's distribution (Guasto 2008; Li & Yoda 2008) or a method of statistical tracking (Guasto *et al.* 2006).

Recently, PIV techniques have been applied to observe fluidic and colloidal dynamics near a solid wall. In these experiments tracer particles are imaged through regular fluorescence microscopy (Joseph & Tabeling 2005) or total internal reflection fluorescence microscopy (TIRFM) (Huang *et al.* 2006; Bouzigues *et al.* 2008; Li & Yoda 2008), in which the depth of observation is approximately 300 nm and allows investigators to directly observe the near-wall region in the nanoscale. However, the finite thickness of the observation depth can bias the experimental results if the tracer particle motion is stochastic with spatially dependent transport properties. One such example is described below.

In the vicinity of a solid wall, a colloidal particle will experience an anisotropic 'hindered' Brownian motion due to an increase of its hydrodynamic drag. This reduced mobility has been reported both theoretically (Brenner 1961; Goldman, Cox & Brenner 1967*a*,*b*; Chaoui & Feuillebois 2003) and experimentally (Bevan & Prieve 2000; Lin, Yu & Rice 2000; Banerjee & Kihm 2005; Oetama & Walz 2006; Huang & Breuer 2007*a*). In most cases, such a spatially dependent hindered mobility leads to difficulties in determining measurement uncertainties, although a few researchers have managed to turn the disadvantages into merits by proposing usage of the hindered Brownian motion to reconstruct near-wall shear flow velocity profile (Hohenegger & Mucha 2007) and to probe the no-slip boundary condition (Lauga & Squires 2005).

There are two equally appropriate approaches that have been used to study the ensemble behaviour of hindered particle motions (Ermak & McCammon 1978). One is the Fokker–Planck approach, which solves the momentum-space partial differential equations to obtain a time evolution of spatial configuration function of the particle ensemble. The other approach is a Langevin simulation, which simulates the motion of each particle in a large ensemble through a stochastic differential equation. In this approach, both deterministic (such as fluid flow, sedimentation and electrostatic repulsion) and stochastic (such as Brownian motion) processes contribute to particle displacements. The overall simulation then yields a spatial distribution of the particle ensemble after each time step. Details provided by this method are not only intuitive in understanding ensemble behaviour but also bear a close resemblance to physical velocimetry experiments. The usefulness of Langevin simulations has been demonstrated in studying the impact of hindered Brownian diffusion on the accuracy of nano-PIV (Sadr, Li & Yoda 2005), on the colloidal particle deposition in a microchannel flow (Unni & Yang 2005) and on the accuracy of potential energy profiles determined via total internal reflection microscopy (Sholl *et al.* 2000).

Using the Fokker–Planck approach, Sadr *et al.* (2007) studied how the hindered Brownian motions of tracer particles normal to the wall could cause bias on accuracy of near-wall velocimetry measurements. While Pouya *et al.* (2008) had presented experimental results that qualitatively support the simulation findings of Sadr *et al.* (2007), these researchers did not consider the effect of fluid shear in their analysis and therefore had overlooked the significant contribution of the shear-related hindered mobility of tracer particles to velocimetry inaccuracy. In this article, we present our simulation and experimental findings that shear effect would dominate over the effect of hindered Brownian motion in a strong shear flow and thus becomes the primary source of velocimetry measurement bias.

Another source of velocimetry inaccuracy that has not yet been examined either theoretically and experimentally is the existence of a near-wall depletion layer of tracer particles due to electrostatic and van der Waals interactions between particles and the wall (Prieve 1999; Guasto 2008; Li & Yoda 2008). In many published studies researchers conveniently assume in near-wall velocimetry data analysis that tracer particles are uniformly distributed without the presence of a depletion layer near wall. However, this is an incorrect assumption that can lead to substantial velocimetry measurement inaccuracy. If a significant portion of the observation depth overlaps with a depletion layer, it causes the ensemble-averaged velocities of near-wall particles to be greatly skewed and therefore significantly deviates from the average fluid velocity in the observed layers. Thus from the perspective of velocimetry accuracy, it is critical to understand how the presence of a particle depletion layer leads to measurement bias.

To better understand and correct such measurement deficiencies we have chosen to investigate near-wall particle dynamics through both Langevin simulations and experimental measurements. We directly examine how the combined effects of hindered diffusion and fluid shear contribute to the skewed near-wall apparent velocity distributions first reported by Jin *et al.* (2004) in their total internal reflection velocimetry (TIRV) experiment, and how such skewed measurements contribute to velocimetry inaccuracy. Furthermore, Derjaguin, London, Verwey and Overbrook (DLVO) theory of particle-wall interactions are incorporated into our Langevin simulations and experimental data analysis to demonstrate the significance of the particle depletion layer in terms of measurement bias. Based on our simulation and experimental results, we propose a data analysis protocol that will enable one to systematically treat the measurement bias and infer the actual near-wall fluid velocities.

In this paper, the theories of near-wall particle dynamics are presented first and followed by a detailed description of the simulation algorithm and experimental procedures. We then discuss the effects of shear hindered Brownian motion and particle-wall interaction and their implications to velocimetry through a comparative analysis of our simulation and experimental results. The paper concludes with a summary of our findings and our thoughts on minimizing inaccuracies of near-wall velocimetry measurements.

2. Theoretical considerations

To examine the accuracy of particle-based velocimetry through both simulations and experiments, it is critical to understand the dynamic theories of near-wall tracer particles, whose translational motions are influenced by local fluid shear force, hindered Brownian motion and particle-wall electrostatic repulsion and van der Waals attractive force. In this section, we introduce the Langevin equation for a charged near-wall particle, and subsequently incorporate all dynamic forces to establish a non-dimensional equation of motion that serves as our basis for experimental data analysis and numerical simulation. Detailed descriptions of the simulation and experimental methodologies are presented in the ensuing sections.

2.1. *The Langevin equation*

In a Langevin simulation, particle displacements are computed based on a stochastic equation (Ermak & McCammon 1978). For a particle in a shear flow as shown in

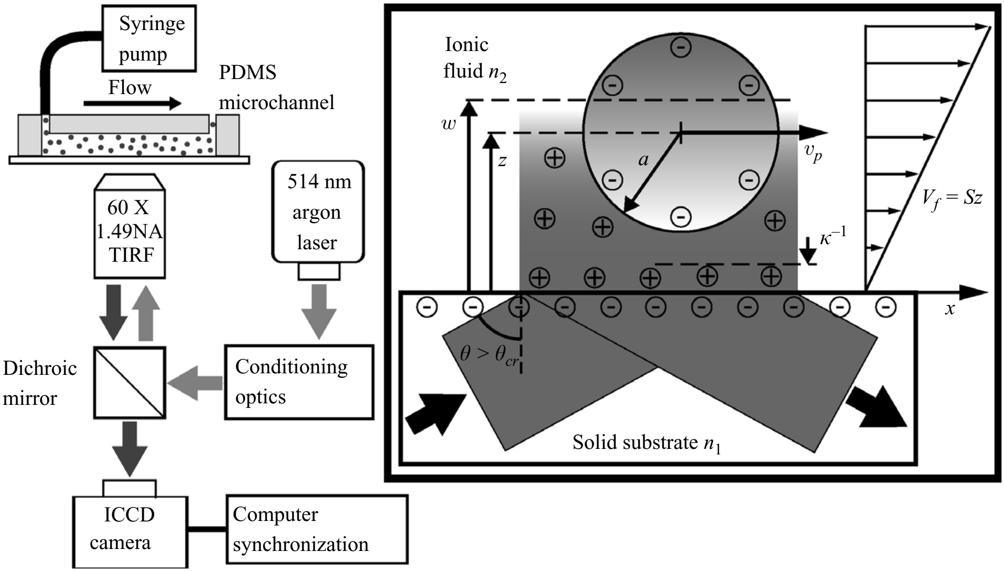

FIGURE 1. A schematic of the simulation geometry and the experimental set-up. A colloidal particle of radius a is freely suspended in a fluid but near a solid wall. The fluid is undergoing a linear shear flow of shear rate S, while the particle translates with a velocity v_p. A no-slip boundary condition is assumed at all fluid/solid wall interfaces. Even though the existence of slip has been reported by Huang *et al.* (2006), its presence would not alter the simulation results and is thus neglected. To measure the motion of a near-wall particle experimentally, an evanescent field is created at the glass-water interface of a poly-dimethyl siloxane (PDMS) microchannel with a penetration depth of approximately 150 nm. This penetration depth, however, is different from the observation depth, which is denoted as w in the figure and is typically a few times larger than the penetration depth. The flow is driven by a syringe pump, and displacement of particles are tracked by imaging the emitted fluorescence using an intensified CCD (ICCD) camera.

figure 1, its displacement between time t_i and t_{i+1} with a time interval of $t_{i+1} - t_i = \delta t$ is

$$x_{i+1} - x_i = v\delta t + \frac{\mathrm{d}D_x}{\mathrm{d}x}\delta t + \frac{D_x}{k_B\Theta}F_x\delta t + N(0, \sqrt{2D_x\delta t}), \tag{2.1a}$$

$$z_{i+1} - z_i = \frac{\mathrm{d}D_z}{\mathrm{d}z}\delta t + \frac{D_z}{k_B\Theta}F_z\delta t + N(0, \sqrt{2D_z\delta t}), \tag{2.1b}$$

where (x, z) is the particle's centre position, v is the translational velocity of the particle due to the shear flow, k_B is the Boltzmann constant and Θ is the fluid temperature. Because particles also undergo Brownian motions, the observed particle velocity v_p, can be different from v. D_x and D_z are the diffusion coefficients in the directions parallel and normal to the wall surface, respectively. In the fluid bulk, or $z \gg a$, both D_x and D_z would be equal to the Stokes–Einstein diffusivity D_0. As it has been mentioned earlier, near-wall particle motion is anisotropic and hindered, and thus $D_x \neq D_z$ and $D_x, D_z \leqslant D_0$. It should be noted that because D_x is only a function of z (Goldman *et al.* 1967*a*), $\mathrm{d}D_x/\mathrm{d}x = 0$ in (2.1*a*). The z-dependency of D_x and D_z is discussed in subsequent sections. F_x and F_z represent external forces acting on the particle in the x and z directions, respectively, and $N(0, \sqrt{2D\delta t})$ denotes the hindered Brownian motion in the form of stochastic particle displacements randomly sampled from a normal distribution with a zero mean and a standard deviation $\sqrt{2D\delta t}$. In a

			Pe			
a (μm)	*G*	S (s^{-1}) =	10^0	10^1	10^2	10^3
0.1	-5.042×10^{-5}		0.0046	0.0463	0.4630	4.630
1.0	-0.5042		4.630	46.30	463.0	4630

TABLE 1. Sample values of the sedimentation coefficient G and the Péclet number Pe for polystyrene particles in aqueous solution ($\Delta\rho = 50$ kg m^{-3}).

simple shear flow scheme there exists no external force in the x direction and $F_x = 0$. In the z direction, however, density mismatch between tracer particles and the fluid can lead to either sedimentation or floatation of the particles. For monodisperse particles with a density greater than that of the suspending fluid, such as polystyrene particles (relative density 1.05) in water, the buoyancy force acting on the particles, F_g, is

$$F_g = \frac{4\pi}{3} a^3 \Delta\rho g, \tag{2.2}$$

where $\Delta\rho$ is the density difference between the tracer particles and the suspending fluid, and g is the gravitational acceleration. Other external forces acting on the particles may also include electrostatic repulsion and van der Waals attraction between particles and the solid boundary surface, and can be calculated from the DLVO theory (Oberholzer, Wagner & Lenhoff 1997).

The equations of motion (2.1*a*) and (2.1*b*) are non-dimensionalized by choosing the particle radius a as the length scale and the time required for an isolated particle to diffuse a distance of one radius a^2/D_0 as the time scale. Therefore (2.1*a*) and (2.1*b*) can be transformed into

$$X_{i+1} = X_i + F(Z_i) \cdot Pe \cdot Z_i \cdot \delta T + N(0, \sqrt{2\beta_x(Z_i)\delta T}), \tag{2.3a}$$

and

$$Z_{i+1} = Z_i + \left.\frac{\mathrm{d}\beta_z}{\mathrm{d}Z}\right|_{Z_i} \delta T + (G + H) \cdot \beta_z(Z_i)\delta T + N(0, \sqrt{2\beta_z(Z_i)\delta T}), \tag{2.3b}$$

where $X \equiv x/a$, $Z \equiv z/a$ and $T \equiv D_0 t/a^2$ are the non-dimensional x, z and t, respectively. The advection and Brownian motion terms are given by

$$F(Z) \equiv \frac{v}{zS}, \quad \beta_x(Z) \equiv \frac{D_x(z)}{D_0}, \quad \beta_z(Z) \equiv \frac{D_z(z)}{D_0},$$

where we have also introduced the fluid shear rate S. Finally, the flow conditions are governed by a Péclet number Pe, a sedimentation coefficient G and a particle-wall interaction coefficient H for electrostatic and van der Waals forces F_{pw}:

$$Pe \equiv \frac{Sa^2}{D_0}, \quad G \equiv \frac{4\pi a^4 g \Delta\rho}{3k_B\Theta}, \quad H(Z) \equiv \frac{F_{pw}(Z)a}{k_B\Theta}.$$

The Péclet number represents the strength of shear compared with that of Brownian motion, while the sedimentation coefficient characterizes the buoyancy force on the particles. Representative values of Pe and G are shown in table 1. Because most near-wall velocimetry measurements utilize submicron tracer particles, all results presented in this paper fall under the regime of $G \ll 1$ where the buoyancy force is much less significant than thermal energy-driven Brownian motion. On the other hand, H

	Δt (ms)			
a (μm)	0.1	1	10	100
0.1	0.022	0.22	2.2	22
1.0	0.000022	0.00022	0.0022	0.022

TABLE 2. Representative values of the non-dimensional time between consecutive image acquisition, ΔT.

can lead to a depletion layer of particles and thus is taken into consideration and discussed in a later section.

Finally, for image-based velocimetry measurements, another important control parameter is the time between consecutive image acquisitions Δt, from which the fluid velocity is estimated. Some sample values of non-dimensional time between consecutive image acquisition, $\Delta T = \Delta t D_0/a^2$, for 1 μm and 100 nm particles are shown in table 2.

2.2. *Effects of shear on particle velocities*

It is well known that shear and near-surface hydrodynamic effects can cause a tracer particle to rotate and translate at a velocity lower than the local fluid velocity in the same shear plane (Goldman *et al.* 1967*b*; Chaoui & Feuillebois 2003). Goldman *et al.* (1967*b*) proposed that the translational velocity v of a particle with radius a in a linear shear flow of a local shear rate S is given by

$$\frac{v}{zS} \equiv F(Z) \simeq 1 - \frac{5}{16}(Z)^{-3}, \tag{2.4}$$

which is valid for large Z, and

$$\frac{v}{zS} \equiv F(Z) \simeq \frac{0.7431}{0.6376 - 0.2\ \ln(Z-1)} \tag{2.5}$$

for small Z. Although there exists no analytical solution for intermediate values of Z, Pierres *et al.* (2001) proposed a cubic approximation to numerical values presented by Goldman *et al.* (1967*b*):

$$\frac{v}{zS} \equiv F(Z) \simeq \left(\frac{1}{Z}\right) \exp\{0.68902 + 0.54756[\ln(Z-1)] + 0.072332[\ln(Z-1)]^2 + 0.0037644[\ln(Z-1)]^3\}. \tag{2.6}$$

In the current simulation, (2.4), (2.6) and (2.5) are used for particles positioned at $(Z-1) \geqslant 1$, $10^{-4} < (Z-1) < 1$ and $(Z-1) \leqslant 10^{-4}$, respectively. Because a particle's translational velocity depends on the shear rate and its distance to the wall, F needs to be updated in (2.1*a*) at every time step of a Langevin simulation.

It has also been suggested that shear-induced lift can be a source of particle migration away from the wall (King & Leighton 1997). However, based on the theory presented by Cherukat & McLaughlin (1994), the shear-induced lift can be shown to be insignificant for micro-and nanoparticles in a low shear flow regime, and thus will be neglected (see Appendix).

2.3. *Hindered Brownian motion*

Near-wall tracer particles are known to exhibit anisotropic hindered Brownian motion due to hydrodynamic effects, and their hindered diffusion coefficient in the direction parallel to the solid surface D_x is (Goldman *et al.* 1967*a*)

$$\frac{D_x}{D_0} \equiv \beta_x(Z) = 1 - \frac{9}{16}(Z)^{-1} + \frac{1}{8}(Z)^{-3} - \frac{45}{256}(Z)^{-4} - \frac{1}{16}(Z)^{-5} + O(Z)^{-6}, \tag{2.7}$$

where this ‘Method of Reflection’ approximation is more accurate for $Z > 2$. For $Z < 2$, Goldman *et al.* (1967*b*) proposed an asymptotic solution:

$$\frac{D_x}{D_0} \equiv \beta_x(Z) = -\frac{2\,[\ln(Z-1) - 0.9543]}{[\ln(Z-1)]^2 - 4.325\,\ln(Z-1) + 1.591}. \tag{2.8}$$

In the direction normal to the wall, the modified diffusion constant D_z was first solved by Brenner (1961) and later simplified by Bevan & Prieve (2000) into the equation

$$\beta_z(Z) = \frac{6(Z-1)^2 + 2(Z-1)}{6(Z-1)^2 + 9(Z-1) + 2}, \tag{2.9}$$

which is much less computationally intensive than the original infinite series solution. Like the particle translational velocity, the dependence of these hindered diffusion coefficients on Z requires them to be updated at every time step of a Langevin simulation.

2.4. *Electrostatic and van der Waals forces*

The electrostatic repulsion F_{el} and the van der Waals force F_{vdw} acting on a suspended particle due to the presence of the wall can be characterized by the DLVO theory (Oberholzer *et al.* 1997). In dimensional terms,

$$F_{el} = 4\pi\epsilon\epsilon_0 a \left(\frac{k_B\Theta}{e}\right)^2 \left(\frac{\hat{\zeta}_p + 4\gamma\Omega\kappa a}{1+\Omega\kappa a}\right)\left[4\tanh\left(\frac{\hat{\zeta}_w}{4}\right)\right]\kappa \mathrm{e}^{-\kappa(z-a)} \equiv B_{pw}\kappa\mathrm{e}^{-\kappa(z-a)}, \tag{2.10}$$

where $\hat{\zeta}_p = e\zeta_p/k_B\Theta$, $\hat{\zeta}_w = e\zeta_w/k_B\Theta$, $\gamma = \tanh(\hat{\zeta}_p/4)$ and $\Omega = (\hat{\zeta}_p - 4\gamma)/2\gamma^3$. Specifically, ϵ is the dielectric constant of the suspending medium, ϵ_0 is the vacuum electrostatic permeability, e is the elementary charge, κ is the inverse of the wall Debye length and ζ_p and ζ_w are the ζ-potentials of the particle and the wall, respectively. The van der Waals force, on the other hand, takes the form of

$$F_{vdw} = \frac{A_{pw}}{6}\left[-\frac{a}{(z-a)^2} - \frac{a}{(z+a)^2} + \frac{1}{z-a} - \frac{1}{z+a}\right], \tag{2.11}$$

where A_{pw} is the Hammaker’s constant for a spherical particle near a flat wall. With $F_{pw} = F_{el} + F_{vdw}$, one can characterize the particle-wall interaction using the constant H:

$$H = \frac{B_{pw}}{k_B\Theta}K\mathrm{e}^{-K(Z-1)} + \frac{A_{pw}}{6k_b\Theta}\left[-\frac{1}{(Z-1)^2} - \frac{1}{(Z+1)^2} + \frac{1}{Z-1} - \frac{1}{Z+1}\right], \tag{2.12}$$

where $K = \kappa a$. Again since H depends on the value of Z, the quantity H needs to be updated at each time step of a simulation.

3. Implementation of Langevin simulations

Since velocimetry experiments are conducted using dilute particle suspensions, our Langevin simulations were conducted under an assumption of no particle–particle interactions. At the beginning of each simulation, a particle was situated at $X = 0$ and placed within a pre-determined range of $1 \leqslant Z \leqslant 10$. In the absence of particle-wall electrostatic and van der Waals interactions, the particle is randomly placed within the pre-determined range. However, in the event that particle-wall interactions were important, initial position of the particle was randomly sampled from a Boltzmann distribution (Jones 2002) based on the DLVO potential.

The simulation then progressed for a total of $\Delta T/\delta T$ steps as prescribed by (2.3*a*) and (2.3*b*), with F, H and β's updated and the position (X, Z) of the particle recorded after each time step. Because the solid wall was located at $Z = 0$, the smallest Z value a particle could have was $Z = 1$, where the particle would be in contact with the wall. A boundary condition was needed in the event that a particle attempted to enter the solid wall during a simulation step. Peters & Barenbrug (2002*a*,*b*) had studied the efficiencies of different boundary conditions for Langevin simulations. Here we chose a simple and yet effective specular reflection to prevent a particle from entering the wall. This is also the only boundary in the simulation geometry as the particle is allowed to move as far away from the solid as Brownian motion takes it. With the time step taken small enough, enforcement of the boundary condition was seldom triggered and less than 0.001 % of the simulated displacements required applications of the boundary condition.

The single particle simulation was then repeated 10^5 times to obtain a large ensemble. It was also repeated for various values of Pe to study its effect. The random number generator, which controls initial particle positions, was seeded identically for all simulation trials to ensure that the results were a consequence of physical parameters only.

Finally, it is important to mention the selection of the size of the computational time step δT, which has two physical constraints (Ermak & McCammon 1978). First, the time step must be much greater than the particle momentum relaxation time $mD_0/k_B\Theta$, where m is mass of one particle. In non-dimensional terms it is equivalent to

$$\delta T \gg \frac{m {D_0}^2}{k_B \Theta a^2} \sim O(10^{-6}), \tag{3.1}$$

for $a > 100$ nm. Second, numerical accuracy requires that the time step must be short enough such that the diffusion coefficients, their gradients and particle hindered mobility are essentially constant during the time step (i.e. $\delta T \ll 1$ for numerical convergence). Therefore δT was chosen to be 10^{-4}, which satisfies both constraints and is numerically efficient.

4. Experimental procedures

4.1. *Materials and optical system*

A schematic of the experimental set-up is shown in figure 1. Flow experiments were carried out in 197 μm × 40 μm × 10 mm, rectangular poly-dimethyl siloxane (PDMS) (Sylgard 184 Silicone Elastomer, Dow Corning) microchannels fabricated by a soft lithography technique (Xia & Whitesides 1998) and mounted on 170 μm thick borosilicate cover glass. The working fluid was pure water (Fluka) with 2.5 mM sodium chloride to reduce the Debye length to approximately 6.1 nm, and thus, reduce the near-wall depletion layer of particles. A low volume fraction (0.01 %) of aqueous polystyrene fluorescent particles (Duke Scientific) were used as tracers. The particles had a mean radius of 100 nm ± 5 % and an emission wavelength of 612 nm. The flow was driven by a syringe pump (Harvard Apparatus) equipped with an accumulator (to damp out oscillations) at a constant flow rate of 1.5 μL min^{-1} ± 0.0035 % for all experiments.

Near-wall tracer particle images were captured using an objective-based TIRFM imaging system (Axelrod 2001). The system was built around a Nikon Eclipse TE2000-U inverted fluorescence microscope with the 514 nm line of an Argon-ion CW laser (Coherent) as the excitation source with a penetration depth of 150 nm. Objective-based TIRFM requires a high numerical aperture objective to achieve an incident angle greater than the critical angle of the fluid–solid interface of the microchannel. For this purpose, we used a CFI Apochromat TIRF 60X oil immersion objective with a numerical aperture of 1.49. Fluorescence images of the particles were captured with an intensified CCD (ICCD) camera (QImaging). The camera is capable of 1360 × 1036 pixels, 12-bit images with an effective pixel size of 161.3 nm at 60X and a minimum inter-frame time Δt of about 1 ms, limited by the decay rate of the intensifier phosphor screen.

4.2. *Particle tracking*

Image pairs were taken at 5 Hz with inter-image acquisition times varying from about 3–43 ms. The polystyrene particle diameters are below their emission wavelength, so the diffraction-limited spot was imaged, which was several hundred nanometres in diameter. Particles were detected by intensity thresholding the maximum pixel value of an image until a possible particle was found. Next, the subpixel x and y locations and peak intensity I were identified by least squares fitting a two-dimensional, Gaussian profile to a 3 × 3 pixel array centred on the maximum intensity pixel (Huang *et al.* 2006). The error in locating a subwavelength particle centre through Gaussian fitting has been shown to be as small as 0.1 pixels for a signal-to-noise ratio (SNR) greater than five (Cheezum, Walker & Guilford 2001). Particle identification was performed for both images of an image pair, and subsequently the identified particles were matched through a nearest neighbour search with window shifting to capture large displacements stemming from long inter-frame times. The low particle concentration helped to minimize misidentification. Once matched, particle displacements (and velocities) were computed for all particles in the 1100 image pairs per trial. Additionally, the the experimental depth of observation was determined by comparing distributions of measured particle intensities to the expected distributions, based on DLVO theory, penetration depth and particle size variation (Guasto 2008). With a constant flow rate (constant velocity) and a fixed exposure time t_e (50 μs), 1100 image pairs were captured at each inter-frame time Δt (3.1, 4.2, 5.6, 7.5, 10.1, 13.5, 18.1, 24.3, 32.5 and 43.6 ms), resulting in 6000–12 000 particle trackings per data set. The tracked particle displacements were decomposed onto a new basis, which lies along the mean measured flow direction to eliminate effects from misalignment of the microchannel to the camera's CCD array.

5. Results and discussions

5.1. *Apparent velocity distributions and inter-image acquisition time*

The apparent particle velocity distributions V_p are examined and shown in figures 2 (Langevin simulation) and 3 (experiment). The apparent velocity V_p of a particle is defined by its displacement ΔX during the time between successive image acquisitions ΔT. In these figures the apparent particle velocity distributions are scaled by the

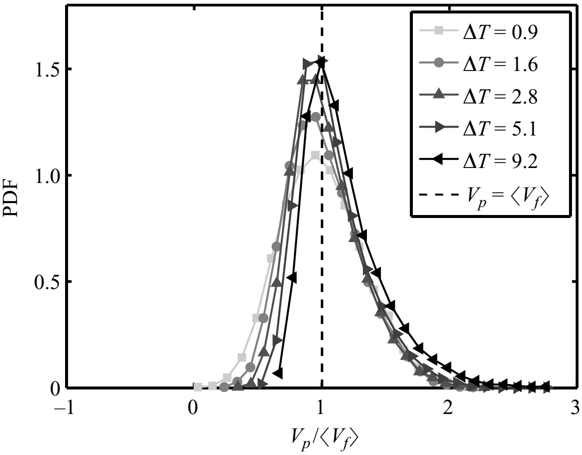

FIGURE 2. The relationship between streamwise apparent velocity distribution and the lengths of time intervals between successive image acquisitions obtained from Langevin simulations. The streamwise apparent velocity distributions are normalized by the average fluid velocity $\langle V_f\rangle$ within the observation depth. All apparent velocity probability density functions (PDFs) are obtained at $Pe = 2.34$ and with particles within the observation depth of $1 \leqslant Z \leqslant 3.5$ at $T = 0$ and $T = \Delta T$. Note that the apparent velocity distribution narrows and skews with increasing inter-acquisition time ΔT. For $\Delta T \ll 1$, the apparent velocity distribution takes the form of a Gaussian distribution.

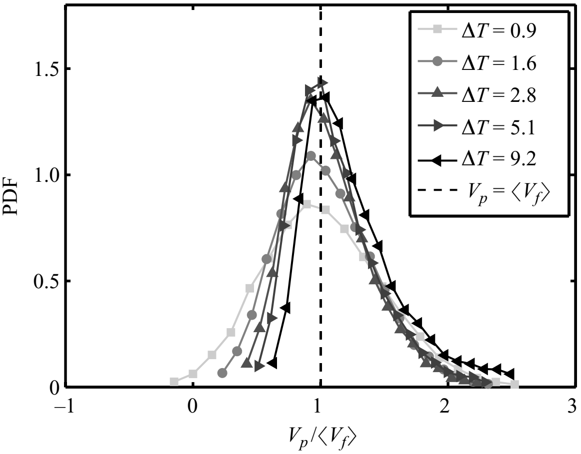

FIGURE 3. The relationship between streamwise apparent velocity distribution and the lengths of time intervals between successive image acquisitions obtained in experimental measurements, with the same parameters as in figure 2. Note that the apparent velocity distribution also narrows and skews with increasing inter-acquisition time ΔT.

average fluid velocity within the same depth of observation, defined by

$$\langle V_f\rangle = \frac{1}{Z_2 - Z_1}\int_{Z_1}^{Z_2} V_f \, \mathrm{d}Z, \tag{5.1}$$

where V_f is the fluid velocity profile and the observation depth is $Z_1 \leqslant Z \leqslant Z_2$.

In figures 2 and 3, one can observe that the apparent particle velocity distributions show remarkably similar shapes between the Langevin simulation and experimental

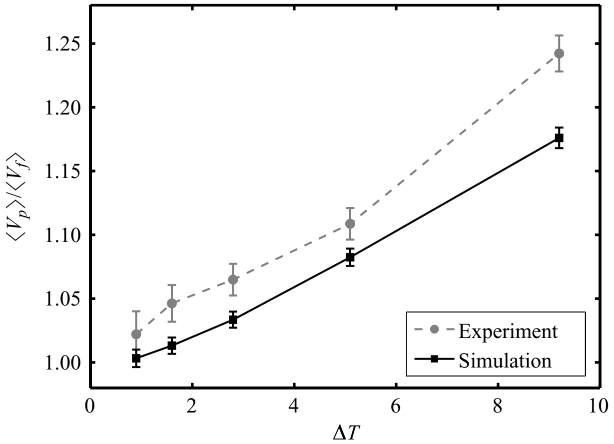

FIGURE 4. The average apparent particle velocity obtained from Langevin simulations (figure 2) and experiments (figure 3). That is, each data point in this figure is the average value of one distribution from either figure 2 or 3. The experimentally measured velocities are slightly higher than the velocities obtained from the simulations by 2 % –5 %. The error bars represent 99 % statistical confidence intervals.

results. Quantitative comparison between the two figures reveals that the mean value of the apparent particle velocity distribution obtained from the Langevin simulation is slightly lower than that of the experimental results, ranging from 2 % at $\Delta T = 0.9$ to 5 % at the highest $\Delta T = 9.2$ (figure 4). Furthermore, for a fixed Pe it is observed in figures 2 and 3 that Brownian motion is dominant at small ΔT, leading to apparent velocity distributions that are Gaussian and significantly wider than that of large ΔT. As ΔT increases, the apparent velocity distributions in both figures narrow due to increasing shear dominance. Such change can be explained by the fact that the width of the averaged Brownian motion velocity V_{BM} scales with $\Delta T^{-1/2}$,

$$\Delta X \sim \sqrt{\Delta T} \quad \Rightarrow \quad V_{BM} = \frac{\Delta X}{\Delta T} \sim \frac{1}{\sqrt{\Delta T}}, \tag{5.2}$$

while the shear-induced flow velocity distribution width scales linearly with ΔT. Thus Brownian motion accounts for a large fraction of the measured apparent velocity at short inter-acquisition time, while the majority of the measured velocity is due to the shear flow at large ΔT. Clearly, if the apparent velocity distributions evolve as a function of inter-acquisition time, the accuracy of particle-based velocimetry must also depend on the length of inter-acquisition time as well.

5.2. *Velocimetry measurement bias due to hindered particle mobility*

The objective of velocimetry is to infer fluid velocities from the measured particle translational velocities V_p. In practice, this is achieved by computing an average velocity of all particles within a depth of observation $Z_1 \leqslant Z \leqslant Z_2$ to estimate the fluid velocity either by finding the maximal correlation value (as used in PIV) or through direct calculation (as used in particle tracking velocimetry (PTV)). We denote this statistical mean velocity of the particle ensemble as $\langle V_p\rangle$. When analysing Langevin simulation or experimental data, $\langle V_p\rangle$ can be computed by

$$\langle V_p\rangle = \frac{\langle \Delta X\rangle}{\Delta T}, \tag{5.3}$$

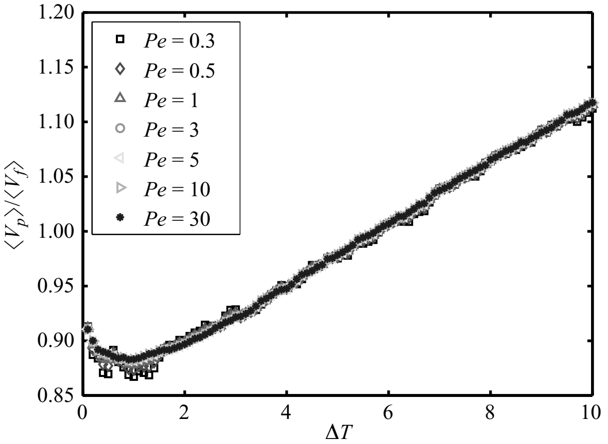

FIGURE 5. The relationship between velocimetry measurement accuracy $\langle V_p\rangle/\langle V_f\rangle$ and the lengths of time intervals between successive image acquisitions obtained from Langevin simulation. The results at various *Pe* for a depth of observation of $1 \leqslant Z \leqslant 3$ are shown. Note that data of all *Pe* collapse onto each other and show a minimum velocity ratio at approximately the same $\Delta T = 1$.

where $\langle \Delta X\rangle$ is the mean displacement of all particles that are present inside the depth of observation at the times of successive image acquisitions. Mathematically, these particles' Z positions must satisfy the requirements that $Z_1 \leqslant Z\,(T = 0) \leqslant Z_2$ and $Z_1 \leqslant Z\,(T = \Delta T) \leqslant Z_2$ in order to be imaged at both image acquisitions of the image pair. Therefore, $\langle V_p\rangle/\langle V_f\rangle$ is the mean values of the scaled apparent velocity distributions shown in figures 2 and 3, and can be interpreted as a measure of velocimetry accuracy, with $\langle V_p\rangle/\langle V_f\rangle = 1$ being the perfect measurement.

The first velocimetry scenario being considered is that of a measurement conducted with uniform particle distribution, where the particle ensemble do not experience any external forces in the direction normal to the wall (i.e. $G = 0$, $H = 0$). The time dependency of the velocimetry accuracy for an observation depth of $1 \leqslant Z \leqslant 3$ in this idealized scenario is shown in figure 5. It can be observed that all $\langle V_p\rangle/\langle V_f\rangle$ ratios exhibit the form of a concave-up function of ΔT, with a minimum occurring at approximately $\Delta T = 1$. Figure 5 also shows that the measurement accuracy is independent of Péclet number, suggesting that changes of flow strength do not significantly affect the velocimetry accuracy. Such observation should not come as a surprise since the fundamental working principle of particle velocimetry is that particle velocities increase or decrease proportionally to the changes in the magnitude of fluid flow. For example, doubling the fluid flow velocity should lead to doubling of measured particle velocities while maintaining the same percentage error. Still, this does not suggest that measurement bias is unaffected by shear as we will demonstrate later in this section. When velocimetry measurement accuracy is compared across different depths of observations $1 \leqslant Z \leqslant W = w/a$, as shown in figure 6, concave-up curves of similar shapes are observed. However, the curves do not fall on top of each other, leading to the conclusion that velocimetry accuracy does depend on the thickness of the observation depth, with increased underestimation of the true velocity occurring for the smallest values of the observation depth W.

Sadr *et al.* (2007) had previously suggested that the velocimetry measurement inaccuracy shown in figure 6 is the result of particles diffusing in and out the depth of

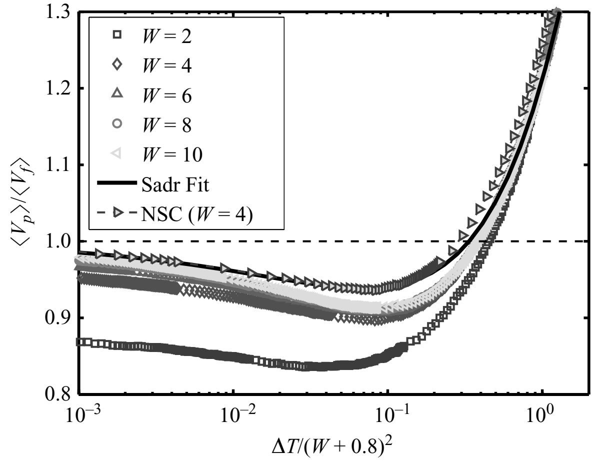

FIGURE 6. Accuracy of the velocimetry derived from Langevin simulations, including one physically inaccurate case where the shear-related hindered mobility of the particles is ignored by assuming $F(Z) = 1$ (denoted 'NSC"). The empirical fit proposed by Sadr *et al.* (2007) is also shown for comparison. The depth of observation is defined as $1 \leqslant Z \leqslant W$, where $W = w/a$. Note that the fit of Sadr *et al.* (2007) closely matches the results of the 'NSC' case. Furthermore, the fit of Sadr *et al.* (2007) predicts the true measurement accuracy very well for large values of $\Delta T/(W + 0.8)^2$ as the curves for all values of W collapse onto each other, while the prediction is much less accurate at $\Delta T/(W + 0.8)^2 \lesssim 0.5$. All data series have the same $Pe = 30$.

observation W between successive image acquisitions (i.e. during ΔT). Thus, a more sensible unit of time for investigating velocimetry accuracy is

$$\frac{\Delta T}{W^2} = \left(\frac{D_0 \Delta t}{a^2}\right)\left(\frac{a^2}{w^2}\right) = \frac{D_0 \Delta t}{w^2}, \tag{5.4}$$

which is equivalent to the typical time scale for a Brownian particle to travel one observation depth w. Sadr *et al.* (2007) explained their findings in that for small ΔT imaged tracer particles are more likely to sample the lower velocity planes, and thus the averaged apparent velocity of the particle ensemble $\langle V_p \rangle$ is lower than the true fluid velocity average $\langle V_f \rangle$. On the other hand at large ΔT there is a higher probability that particles can sample velocity planes farther away from the surface and still manage to return to the depth of observation at the time of second image acquisition. Such excursions bias the observed particle displacements, leading to erroneously large values of the particle translational velocity and thus overestimating the fluid velocity. Sadr *et al.* (2007) further suggested that by rescaling ΔT with $(W + 0.8)^2$, the curves of $\langle V_p \rangle / \langle V_f \rangle$ ratios would collapse onto each other and they offer a numerical model that can estimate measurement accuracy within 7 % for all ΔT. To compare their finding with our Langevin simulation results, the velocimetry accuracy (figure 6) is plotted using the proposed alternative time scale of Sadr *et al.* (2007) and compared with their numerical fit. In figure 6 it can be observed that for large values of $\Delta T/(W + 0.8)^2$ the velocimetry accuracy curves collapse onto each other and the numerical model of Sadr *et al.* (2007) predicts the velocimetry accuracy very well, while the curves still diverge at lower values of $\Delta T/(W + 0.8)^2$ and the fit of Sadr *et al.* (2007) overestimates the velocimetry accuracy. Because Sadr *et al.* (2007) examined only the effect of hindered particle Brownian motion on velocimetry accuracy, the closeness of their numerical fit to our simulation data curves at large $\Delta T/(W+0.8)^2$ implies that under this range of time scale hindered Brownian motion and the excursion of the particles outside the observation depth are the main sources of velocimetry bias. On the other hand, the overestimation of their numerical model on the measurement accuracy at small $\Delta T/(W+0.8)^2$ suggests that under this time scale the bias is not solely dominated by hindered Brownian motion, and shear-related hindered mobility of the particles also contributes significantly. The significance of the shear-related hindered mobility is further supported by the fact that in figure 6 the results of the 'NSC' case, which ignores any shear-related corrections in particle translation by assuming $F(Z)=1$, closely match the fitted curve of Sadr *et al.* (2007). Because both of these cases unrealistically ignore the shear-related effects, they produce predictions of much higher velocimetry accuracies than the actual values. In figure 6 one can observe that the deviation between our simulation results and the fit of Sadr *et al.* (2007) for $\Delta T/(W+0.8)^2 \lesssim 0.5$ grows larger as W becomes smaller. Such a trend suggests that the role of shear-related hindered mobility on velocimetry measurement bias becomes more prominent when the depth of observation is set closer to the solid wall.

Our simulation findings also offer an analytical algorithm from which the true fluid velocity can be estimated more accurately than from the correction curve that Sadr *et al.* (2007) proposed. First, the velocimetry bias can be estimated by

$$\frac{\langle V_p\rangle}{\langle V_f\rangle} = \left(\frac{\langle V_p\rangle}{\langle V_{ps}\rangle}\right)\left(\frac{\langle V_{ps}\rangle}{\langle V_f\rangle}\right), \tag{5.5}$$

where $\langle V_{ps}\rangle$ is the mean velocity of a uniformly distributed particle ensemble inside a depth of observation $Z_1 \leqslant Z \leqslant Z_2$, if particles do not experience Brownian motion and only the shear-related hindered mobilities of the particles are considered. Mathematically, in a linear shear flow $\langle V_{ps}\rangle$ can be computed by

$$\langle V_{ps}\rangle = \frac{Pe}{Z_2 - Z_1}\int_{Z_1}^{Z_2} F(Z)\cdot Z\,\mathrm{d}Z, \tag{5.6}$$

where $F(Z)$ is the shear-related hindered particle mobility as described in §2. Therefore,

$$\frac{\langle V_{ps}\rangle}{\langle V_f\rangle} = \frac{Pe}{\langle V_f\rangle(Z_2 - Z_1)}\int_{Z_1}^{Z_2} F(Z)\cdot Z\,\mathrm{d}Z, \tag{5.7}$$

which can be easily calculated using (2.4), (2.5), (2.6) and (5.1) for the desired range of Z. The values of $\langle V_p\rangle/\langle V_{ps}\rangle$, on the other hand, can be obtained from our Langevin simulations. The values of $\langle V_p\rangle/\langle V_{ps}\rangle$ are found to exhibit a time scale similarity, as demonstrated by all curves of $\langle V_p\rangle/\langle V_{ps}\rangle$ for various depths of observation collapsing closely onto each other when plotted against T/W^2 in figure 7. The curves of $\langle V_p\rangle/\langle V_{ps}\rangle$ can be closely fitted by a numerical model first suggested by Sadr *et al.* (2007),

$$\frac{\langle V_p\rangle}{\langle V_{ps}\rangle} \approx A + (1-A)\exp\left(-B\sqrt{\frac{T}{W^2}}\right) + C\sqrt{\frac{T}{W^2}}. \tag{5.8}$$

By fitting equation (5.8) to the values of $\langle V_p\rangle/\langle V_{ps}\rangle$ for $1 \leqslant Z \leqslant 2$ using a least square of residual method, we found that $A=0.43$, $B=1.85$ and $C=0.63$, and the resulting fit predicts the $\langle V_p\rangle/\langle V_{ps}\rangle$ values of all depths of observation to within 3 %. Thus by combining (5.5), (5.7) and (5.8), an appropriate correction factor to $\langle V_p\rangle$ can be obtained to estimate the true fluid velocity with a less than 3 % inaccuracy.

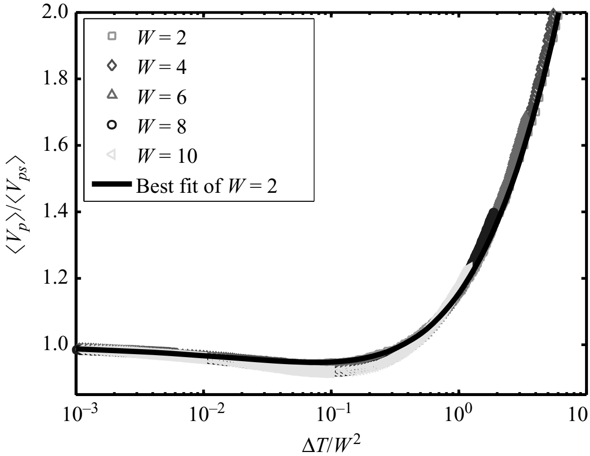

FIGURE 7. The dependency of $\langle V_p \rangle / \langle V_{ps} \rangle$ on the lengths of time intervals between successive image acquisitions, calculated based on the results of Langevin simulations. Because $\langle V_{ps} \rangle$ takes the shear-related effect into consideration, $\langle V_p \rangle / \langle V_{ps} \rangle$ represents the measurement inaccuracy resulted from hindered Brownian motion of particles. The measurement accuracy curves for all observation ranges of $1 \leqslant Z \leqslant W$ show a scaling similarity under a time scale of $\Delta T / W^2$. A least square residual fit of (5.8) to the data of $W = 2$, denoted 'Best fit of $W = 2$', is found to predict $\langle V_p \rangle / \langle V_{ps} \rangle$ to within 3 % of the actual values for all W.

5.3. *Velocimetry measurement bias due to the presence of a particle depletion layer*

The accuracy of particle-based velocity measurements can be further compromised if there exists a sampling bias of the fluid velocities due to a non-uniform distribution of particles. Specifically, it has been a common practice in reported near-wall velocimetry studies to complete data analysis by assuming that tracer particles are uniformly distributed within the observation depth, while not being aware of the potential sampling bias existing in the system. A common mis-sampling of this sort in almost all aqueous fluids is due to electrostatic and van der Waals forces between particles and the wall as described in § 2.4. To demonstrate that our Langevin simulation can accurately capture such particle-wall interactions (i.e. $H \neq 0$) based on the DLVO theory, a trial simulation was conducted with an initially uniform particle concentration distribution in the wall-normal direction. Periodic samplings of the particle distribution profile at various time T are shown in figure 8, and it is observed that the spatial distribution of a particle ensemble that start out uniformly evolves with time and eventually settles into a steady, non-uniform spatial distribution after a transient period, with the final spatial distribution agreeing with the Boltzmann distribution prediction based on the DLVO theory. Note that there is both a depletion layer (approximately $Z \leqslant 1.5$ for the presented case in figure 8), induced by electrostatic repulsion, followed by a near-wall peak, induced by the van der Waals attractive forces, before the concentration settles to the bulk value. These results support the notion that the DLVO–Boltzmann distribution is the steady-state concentration profile of a particle ensemble experiencing electrostatic and van der Waals interaction with the wall. But more importantly the depletion layer will lead to a significant bias in any estimated velocity distribution, as very slow-moving particles near the wall will be underrepresented, while there will be an excess sampling of the shear plane corresponding to the DLVO peak.

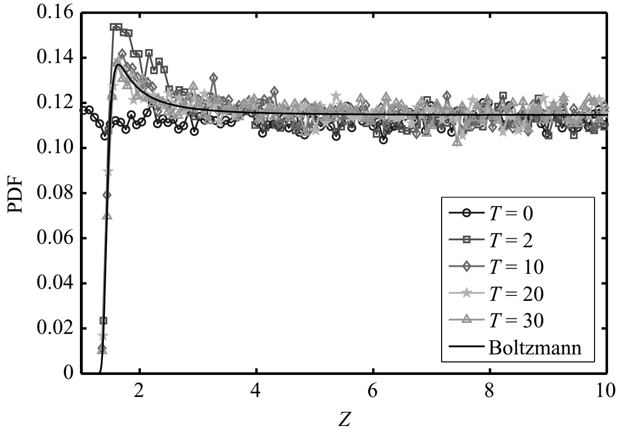

FIGURE 8. Simulated spatial distribution of particles at $K = 16.33$, which is equivalent to a 100 nm-radius polystyrene particle (density 1050 kg m^{-3}) suspended in water of 2.5 mM ionic concentration with a Debye length of 6.1 nm. The particles are initially uniformly distributed in the volume ($1 \leqslant Z \leqslant 10$) at $T = 0$ and allowed to translate due to Brownian motion, electrostatic repulsion and van der Waals force. The motion of the particles are confined to only within this volume for mass conservation. Note that the spatial distribution of the particles settles into the Boltzmann distribution after a transient period ($T \approx 10$).

A full Langevin simulation incorporating DLVO interactions ($H \neq 0$) was conducted and compared with experimental measurements to investigate its effect. In this simulation, particles are initially seeded according to the DLVO–Boltzmann distribution shown in figure 8 by assuming that the particle ensemble has reached the spatially steady state. The rest of the simulation steps follow that of §2, with particles experiencing hindered Brownian motion, electrostatic and van der Waals forces at each time step. The simulation was conducted using Debye length and Péclet number identical to that of the experimental conditions described in §4.1 for comparison. The experimental and simulation results are compared and shown in figures 9, 10 and 11. In figure 9, the velocimetry accuracy parameter $\langle V_p \rangle / \langle V_f \rangle$ is plotted against the time between image acquisitions ΔT for simulations with and without a DLVO depletion layer and compared with experimental measurements. The velocimetry accuracy curves for both cases of simulations show a similar tendency of starting out at a constant level, subsequently decreasing to a global minimum, and finally increasing unboundedly with increasing ΔT. However, a large gap exists between the two curves, suggesting that failure to consider the depletion layer can lead to substantial measurement bias. In fact, for the depth of observation ($1 \leqslant Z \leqslant 3.5$) under consideration, the particle depletion layer always leads to an overestimation of fluid velocity, as the curve of DLVO depletion layer stays above the line of $\langle V_p \rangle / \langle V_f \rangle = 1$. Also shown in figure 9 is that our experimental results closely match that of simulations with a DLVO depletion layer, further confirming that a particle depletion layer exists near a charge solid wall and require significant attention during velocimetry data analysis.

In figure 10, the velocimetry accuracy parameter is plotted against the time between image acquisitions ΔT for different depths of observation. A unique feature in the presence of DLVO interaction is that the ratio of $\langle V_p \rangle / \langle V_f \rangle$ is always larger than unity for small ΔT. In fact, for depth of observation very close to the wall (i.e. small W), the ratio of $\langle V_p \rangle / \langle V_f \rangle$ stay above unity for all ΔT, suggesting that such near-wall particle

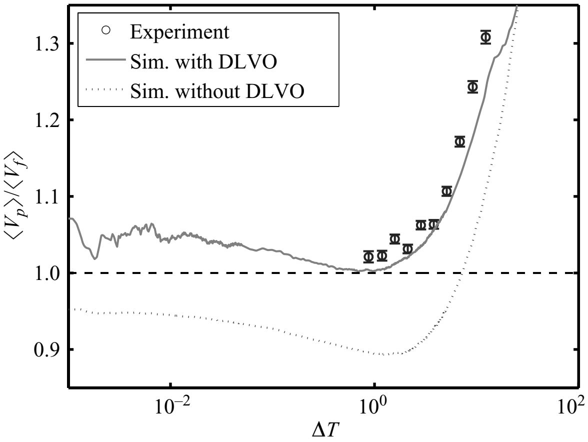

FIGURE 9. Contribution of the particle depletion layer to velocimetry measurement bias. Velocimetry accuracies $\langle V_p \rangle / \langle V_f \rangle$ from a Langevin simulation with and without incorporating the DLVO theory, and experimental measurements are plotted and compared. Significant differences between the two types of simulations are observed and the experimental measurement results closely match the results of Langevin simulation with a DLVO depletion layer. All data series, including simulations and experiments, have $Pe = 2.34$ and a depth of observation of $1 \leqslant Z \leqslant 3.5$.

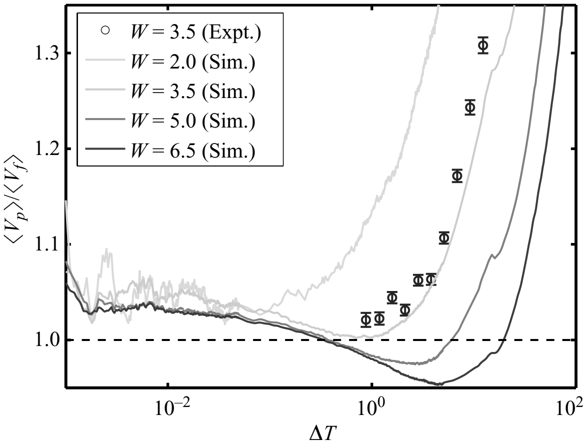

FIGURE 10. The dependency of velocimetry accuracy $\langle V_p \rangle / \langle V_f \rangle$ on the lengths of time intervals between successive image acquisitions obtained from both Langevin simulation and experimental measurements. In both cases, particles experience hindered Brownian motion, DLVO particle-wall interactions and shear flow during their motions. The depth of observation is defined as $1 \leqslant Z \leqslant W$. Note that the depth of observation in our experimental measurements is $1 \leqslant Z \leqslant 3.5$. All data series, including simulations and experiments, have $Pe = 2.34$.

velocimetry measurements will always overestimate the actual fluid velocity within this region. This can be explained by the significant overlapping of the observation depth and the near-wall particle depletion layer, whose presence leads to bias sampling of near-wall velocities and underrepresentation of the low fluid velocities near-wall in the velocity distribution statistics. One significant area in which this bias may have significant repercussions is in the use of particle velocimetry to estimate fluid slip velocities near surfaces (Joseph & Tabeling 2005; Huang *et al.* 2006; Huang & Breuer

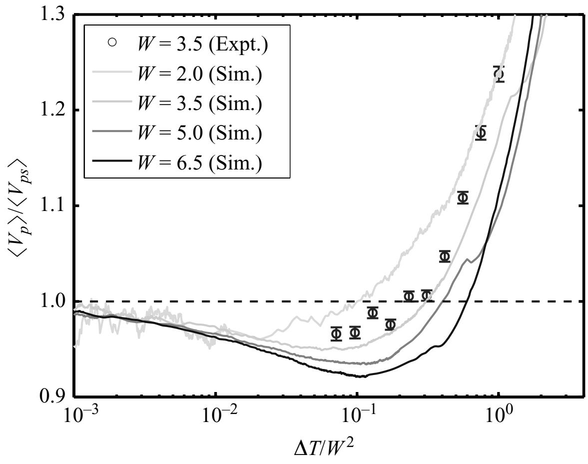

FIGURE 11. Velocimetry accuracies from both Langevin simulations and experimental measurements, with a rescaled non-dimensional time $\Delta T/W^2$ and the shear-related effect on particles taken into consideration by $\langle V_p\rangle/\langle V_{ps}\rangle$ as discussed in § 5.2 and (5.6). The measurement accuracy curves for all observation ranges of $1 \leqslant Z \leqslant W$ again show a scaling similarity, particularly for $\Delta T/W^2 \leqslant 0.02$. All data series have $Pe = 2.34$.

2007*b*; Bouzigues *et al.* 2008). For instance, in our own previous studies of fluidic slip (Huang *et al.* 2006; Huang & Breuer 2007*b*), as $W \approx 3.5$ and $\Delta T \approx 1$, we estimate a maximum of 3 % additional error in slip velocity measurements should be assumed based on the plots of figure 10. We recommend that future measurements should explicitly estimate the velocimetry bias effects reported in this paper.

To further understand the effects of hindered Brownian motion, the presence of the wall, and the electrostatic and van der Waals forces, the shear effect on particles and the spatial distribution of the particle ensemble are taken into consideration by plotting $\langle V_p\rangle/\langle V_{ps}\rangle$ against a rescaled non-dimensional time $\Delta T/W^2$ in figure 11. Here again we observe scaling similarity for all curves, particularly for $\Delta T/W^2 \leqslant 0.02$. In contrast to figure 10, the values within this region of rescaled non-dimensional time remain less than unity. This suggests that proper consideration of near-wall particle depletion layer during data analysis can reduce overestimation of fluid velocity. For $\Delta T/W^2 > 0.02$, however, the curves for different W values do not collapse as completely as the curves in figure 7 do. This is most likely due to the different ratios of depletion layer thickness to the depth of observation for different curves. This is confirmed by the fact that as the values of W increases, the curves of $\langle V_p\rangle/\langle V_{ps}\rangle$ begin to fall closer and closer to each other. Still, the method to obtain a better fluid velocity estimate described in § 5.2, namely (5.5), can still be applied to improve velocimetry accuracy. Such an operation can be achieved by using the values of $\langle V_p\rangle/\langle V_{ps}\rangle$ obtained from curves such as those shown in figure 11, and by incorporating the DLVO–Boltzmann distribution of the particles, $C(Z)$, to modify (5.7) into

$$\left(\frac{\langle V_{ps}\rangle}{\langle V_f\rangle}\right) = \frac{Pe}{\langle V_f\rangle (Z_2 - Z_1)} \int_{Z_1}^{Z_2} F(Z) \cdot C(Z) \cdot Z \, \mathrm{d}Z. \qquad (5.9)$$

Again by combining (5.5), (5.8) and (5.9), an appropriate correction factor to $\langle V_p\rangle$ can be obtained.

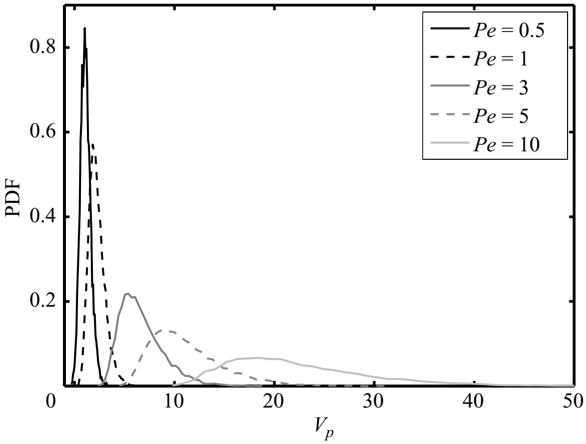

FIGURE 12. Apparent velocity distribution of simulated particles remaining in the observation range $1 \leqslant Z \leqslant 3$ after $\Delta T = 10$. Larger *Pe* leads to an apparent velocity distribution with larger mean, width and skewness.

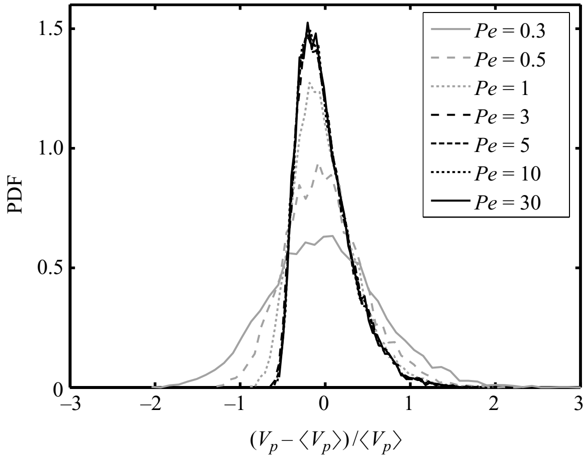

FIGURE 13. Rescaled apparent velocity distribution of simulated particles remaining in the observation range $1 \leqslant Z \leqslant 3$ after $\Delta T = 10$. $\langle V_p \rangle$ is the mean value of each apparent velocity PDF. The rescaled PDF's collapse onto each other at *Pe*3. In general, larger *Pe* has a narrower but more skewed distribution.

5.4. *Apparent velocity distribution skewness and shear*

Another useful feature of a two-dimensional Langevin simulation is the ability to investigate the effects of shear and random (Brownian) motion on apparent velocity distributions analysed in the context of Péclet numbers *Pe*. Shown in figure 12 is the distribution of non-dimensional apparent velocity, $V_p = \Delta X/\Delta T$, for ensembles of particles subject to different Péclet numbers. One can observe that the apparent velocity PDFs widen and skew as the shear rate increases, in good agreement with the experimentally measured PDFs reported by Jin *et al.* (2004) and Huang *et al.* (2006).

Upon further analysis, it is observed that, by scaling with the ensemble average velocity $\langle V_p \rangle$, the apparent velocity PDFs collapse onto a single distribution for $Pe > 3$, as shown in figure 13. The collapsed PDFs for $Pe > 3$ have a smaller

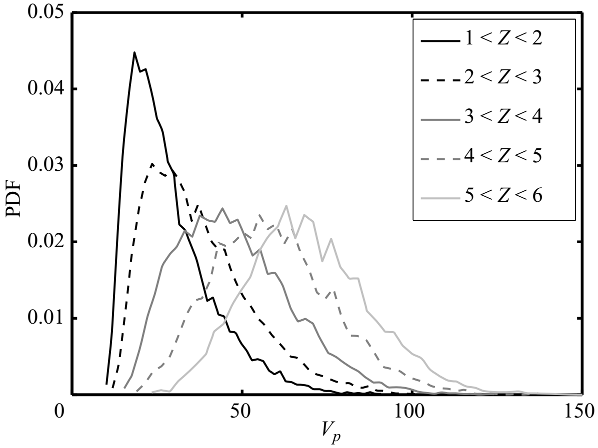

FIGURE 14. Apparent velocity distribution of simulated particles at various depths of observation. All apparent velocity distributions are obtained at $\Delta T = 10$ and $Pe = 10$. Particles that start off farther away from the surface move faster because they are carried by fluids at higher velocity planes, and their distributions are more symmetric due to less influence of the wall and hindered Brownian motion.

distribution width but a more pronounced skewness, while the rescaled distributions of $Pe < 3$ are wider but more symmetric. Such scaling characteristics can be understood by drawing analogy with the theory of Taylor dispersion. As in Taylor dispersion, the case of $Pe < 1$ represents the streamwise diffusion overpowers over the convection transport and cross-stream diffusion of particles. Therefore velocity distributions measured based on particle translations would be dominated by the streamwise diffusion whose relative magnitude increases with decreasing Péclet number, leading to the large distribution widths for small Pe shown in figure 13. For $Pe > 3$ where the assumption of $Pe \gg 1$ for Taylor dispersion is met, the width of a velocity distribution σ scales with the particle dispersion parallel to the flow:

$$\sigma \sim \sqrt{\langle (V_p - \langle V_p \rangle)^2 \rangle} \sim \sqrt{\langle (\Delta X - \langle \Delta X \rangle)^2 \rangle} \sim \sqrt{K} \sim Pe, \tag{5.10}$$

where K is the Taylor diffusivity (Deen 1998). Since the average particle velocity $\langle V_p \rangle$ also scales with Pe, the width of a normalized velocity distribution $(V_p - \langle V_p \rangle)/\langle V_p \rangle$ shown in figure 13 must scale with

$$\sigma_N = \frac{\sigma}{\langle V_p \rangle} \sim \frac{Pe}{Pe} = 1. \tag{5.11}$$

That is, for large Péclet number the normalized velocity distribution width is independent of Péclet number due to Taylor dispersion. Indeed such dispersion behaviour was also observed in experimental results reported by Huang *et al.* (2006), and the agreement of the current Langevin simulation further validates the presented physical arguments.

The sources of apparent velocity distribution skewness are the hindered Brownian motion of the particles and more importantly, the presence of the wall. One can observe in figure 14 that the apparent velocity PDFs for observation ranges farther away from the wall are wider and less skewed than those obtained from observation ranges closer to the wall. When an observation range is set to be far way from the wall, the targeted particle ensemble is equally likely to sample fluid velocities that are both above and below the particle's initial position within the observation range, leading to a more symmetric apparent velocity distributions. However, for particle ensembles that are close to the wall, such symmetric sampling is broken as the particles are unable to penetrate the wall and therefore are more likely to sample velocities at shear planes above the depth of observation. As a result, the apparent velocity PDF has an asymmetric shape with a long positive tail coming from the bias in sampling higher shear planes. Also contributing to the skewness are the hindered Brownian motion and the shear-related hindered mobility of particles in the near-wall region, while far away from the wall, their effects are less experienced.

The skewness of apparent velocity distributions could further lead to undesirable velocimetry inaccuracy, particularly in the case of PIV which obtains an ensemble-averaged displacement by searching for the most probable particle translation through cross-correlation of several particles imaged in acquisitions. Statistically, the correlation-based ensemble averaged displacement represents the particle displacement that occurs most frequently, or the *mode* of particle displacement. This is in contrast to using the statistical average, or the *mean* of the particle displacements to calculate the ensemble velocity usually accomplished in PTV. Because the apparent velocity distributions of the near-wall regions have long positive tails, as demonstrated in figure 14, their statistical mean values will always be greater than the values of the distribution modes. Referring back to figure 6, at $\Delta T/(W+0.8)^2 \lesssim 0.5$, PIV would then underestimate the true fluid velocity more than PTV would as in this region the obtained $\langle V_p\rangle/\langle V_f\rangle$ is less than one, and thus PTV would be more accurate than PIV under this time scale. At $\Delta T/(W+0.8)^2 > 0.5$, on the other hand, PTV would overestimate the true fluid velocity than PIV, suggesting that PIV might be the more accurate for this time scale. However, such an improvement in measurement accuracy could be offset by the fact the PIV algorithm is insensitive to particle drop-in and drop-out between image acquisitions, and this can become a significant source of bias at large ΔT. Such reasoning suggests that PTV is probably a more accurate method for near-wall velocity measurements under most circumstances.

6. Concluding remarks

Through Langevin simulations and direct experimental measurements, we demonstrate that shear-related hindered mobility of near-wall particles, previously not considered, can contribute to near-wall velocimetry bias with as much influence as much as the effects of hindered Brownian motion. In addition, we have shown that the non-uniform distribution of particles near a wall due to electrostatic and van der Waals forces is also a significant source of measurement inaccuracy that cannot be ignored. In both cases, our results suggest an analytical method to obtain a better estimate of the true fluid velocity through a combination of 'velocimetry accuracy curves' and theoretical calculation of the hindered mobility and concentration profile of near-wall particles. The protocol for a linear fluid velocity profile is summarized as the following:

(i) From PTV data, compute $\langle V_p\rangle$, the mean apparent velocity of the tracer particles.

(ii) With a prior knowledge of the velocity profile model, calculate

$$\Phi = \frac{1}{Z_2 - Z_1}\int_{Z_1}^{Z_2} V(Z)\,\mathrm{d}Z,$$

where $V(Z) = Z$ is the velocity profile model. Z_1 and Z_2 are the positions of the observation depth low and upper boundaries, respectively. Φ is a single numerical value.

(iii) Calculate

$$\Psi = \frac{1}{Z_2 - Z_1} \int_{Z_1}^{Z_2} F(Z) \cdot C(z) \cdot V(Z)\,\mathrm{d}Z$$

where $F(Z)$ is computed using the velocity profile model $V(Z)$ inside the observation depth and $C(Z)$ is the initial particle concentration profile. Ψ is also a single numerical value.

(iv) Calculate the following quantity based on measurement parameters:

$$\Pi = 0.43 + (1 - 0.43)\exp\left(-1.85\sqrt{\frac{T}{W^2}}\right) + 0.63\sqrt{\frac{T}{W^2}}.$$

(v) The true fluid velocity can be estimated using

$$\langle V_f \rangle = \left(\frac{\Phi}{\Pi\Psi}\right)\langle V_p \rangle.$$

For nonlinear velocity profile models, the velocimetry correction factor $(\Phi/\Pi\Psi)$ should not be obtained through the prescribed steps listed above as a linear $V(Z)$ is implicitly assumed in $F(Z)$ and Π. However, the velocimetry correction factor can be numerically obtained by running a Langevin simulation with the same procedure described in this paper and incorporating the nonlinear velocity profile models. Examples of nonlinear profiles include parabolic and exponential profiles for a pressure driven flow and an electro-osmotic flow, respectively.

Finally, we note that correlation-based methods, such as PIV, will fundamentally have a difficult time achieving accurate results. PTV approaches should tend to be more successful, although they require low seeding densities in order to achieve reliable particle–particle matching and thus might be more time consuming. An approach that allows for high particle seeding densities while still obtaining an ensemble velocity distribution is the statistical particle tracking velocimetry (SPTV) (Guasto *et al.* 2006) which is ideal for this class of flows. Apparent velocities obtained from SPTV measurements can be corrected using the algorithm outlined in the results and discussion section to minimize diffusion and wall-induced measurement bias.

This work was supported by a cooperative research programme funded by Sandia National Laboratory and the National Science Foundation.

Appendix. Lack of shear-induced lift force on near-wall submicron particles

It has been suggested that a shear-induced lift force can act on suspended particles in a linear shear flow, making them more likely to move away from a solid boundary. This would result in a non-uniform distribution of particles near wall where velocimetry measurements take place. However, we believe that such a lift force is insignificant for submicron particles, and in this Appendix, an established theory is presented to support our argument.

The subject of lift forces acting on a small sphere in a wall-bounded linear shear flow has been thoroughly studied by Cherukat & McLaughlin (1994). Here we will present only the theory that applies to the flow conditions under consideration. Suppose that a free-rotating rigid sphere of radius a is in a Newtonian incompressible fluid of kinematic viscosity ν and is in the vicinity of a solid wall. In the presence of a linear shear flow, the free-rotating sphere travels at a velocity v_p that is different from the local fluid velocity v_f. We can define a characteristic Reynolds number based on the velocity difference $v_p - v_f$ with

$$Re_L = \frac{(v_p - v_f)\,a}{\nu}. \tag{A 1}$$

Another characteristic Reynolds number based on shear rate can be defined as

$$Re_S = \frac{Sa^2}{\nu}, \tag{A 2}$$

where S is the wall shear rate. In this geometry, the wall can be considered as located in the 'inner region' of flow around the particle if $Re_L \ll Z^{-1}$ and $Re_S \ll Z^{-2}$, where $Z \equiv z/a$ and z is the distance between the particle's centre and the wall. For near-wall particle velocimetry described in this paper, $Re_L \sim Re_S \sim 10^{-7}$ while $Z^{-1} \sim O\,(1)$, and thus the inner region theory of lift force applies.

For a flat wall located in the inner region of flow around a free-rotating particle, the lift force F_L which is perpendicular to the wall, is scaled by (Cherukat & McLaughlin 1994)

$$F_L \sim Re_L \cdot I, \tag{A 3}$$

where I is a coefficient that can be numerically estimated by

$$\begin{aligned} I = {} & [1.7631 + 0.3561Z^{-1} - 1.1837Z^{-2} + 0.845163Z^{-3}] \\ & - [3.21439Z + 2.6760 + 0.8248Z^{-1} - 0.4616Z^{-2}]\left(\frac{Re_S}{Re_L}\right) \\ & + [1.8081 + 0.879585Z^{-1} - 1.9009Z^{-2} + 0.98149Z^{-3}]\left(\frac{Re_S}{Re_L}\right)^2 . \end{aligned} \tag{A 4}$$

Again for the velocimetry conditions described in this paper, $I \sim O\left(10^2\right)$. Therefore

$$F_L \sim Re_L \cdot I \lesssim (10^{-7})\left(10^2\right) \ll 1, \tag{A 5}$$

and the lift force acting on near-wall particles is insignificant and can be neglected for all practical purposes.

REFERENCES

Axelrod, D. 2001 Total internal reflection fluorescence microscopy in cell biology. *Traffic* **2**, 764–774.

Banerjee, A. & Kihm, K. D. 2005 Experimental verification of near-wall hindered diffusion for the Brownian motion of nanoparticles using evanescent wave microscopy. *Phys. Rev.* E **72**, 042101.

Bevan, M. A. & Prieve, D. C. 2000 Hindered diffusion of colloidal particles very near to a wall: revisited. *J. Chem. Phys.* **113**, 1228–1236.

Bouzigues, C. I., Tabeling, P. & Bocquet, L. 2008 Nanofluidics in the debye layer at hydrophilic and hydrophobic surfaces. *Phys. Rev. Lett.* **101**, 114503.

Brenner, H. 1961 The slow motion of a sphere through a viscous fluid towards a plane wall. *Chem. Engng Sci.* **16**, 242–251.

Chaoui, M. & Feuillebois, F. 2003 Creeping flow around a sphere in a shear flow close to a wall. *Quart. J. Mech. Appl. Math.* **56**, 381–410.

Cheezum, M. K., Walker, W. F. & Guilford, W. H. 2001 Quantitative comparison of algorithms for tracking single fluorescent particles. *Biophys. J.* **81**, 2378–2388.

Cherukat, P. & McLaughlin, J. B. 1994 The inertial lift on a rigid sphere in a linear shear flow field near a flat wall. *J. Fluid Mech.* **263**, 1–18.

Deen, W. M. 1998 *Analysis of Transport Phenomena*. Oxford University Press.

Ermak, D. L. & McCammon, J. A. 1978 Brownian dynamics with hydrodynamic interactions. *J. Chem. Phys.* **69**, 1352–1360.

Goldman, A. J., Cox, R. G. & Brenner, H. 1967*a* Slow viscous motion of a sphere parallel to a plane wall – I: motion through a quiescent fluid. *Chem. Engng Sci.* **22**, 637–651.

Goldman, A. J., Cox, R. G. & Brenner, H. 1967*b* Slow viscous motion of a sphere parallel to a plane wall – II: Couette flow. *Chem. Engng Sci.* **22**, 653–660.

Guasto, J. S. 2008 Micro- and nano-scale colloidal dynamics near surfaces. PhD thesis, Brown University, Providence, RI.

Guasto, J. S. & Breuer, K. S. 2009 High-speed quantum dot tracking using evanesent wave illumination. *Exp. Fluids* (in press).

Guasto, J. S., Huang, P. & Breuer, K. S. 2006 Statistical particle tracking velocimetry using molecular and quantum dot tracer particles. *Exp. Fluids* **41**, 869–880.

Hohenegger, C. & Mucha, P. J. 2007 Statistical reconstruction of velocity profiles for nanoparticle image velocimetry. *J. Appl. Math.* **68**, 239–252.

Huang, P. & Breuer, K. S. 2007*a* Direct measurement of anisotropic near-wall hindered diffusion using total internal reflection velocimetry. *Phys. Rev.* E **76**, 046307.

Huang, P. & Breuer, K. S. 2007*b* Direct measurement of slip length in electrolyte solutions. *Phys. Fluids* **19**, 028104.

Huang, P., Guasto, J. S. & Breuer, K. S. 2006 Direct measurement of slip velocities using three-dimensional total internal reflection velocimetry. *J. Fluid Mech.* **566**, 447–464.

Jin, S., Huang, P., Park, J., Yoo, J. Y. & Breuer, K. S. 2004 Near-surface velocimetry using evanescent wave illumination. *Exp. Fluids* **37**, 825–833.

Jones, R. A. L. 2002 *Soft Condensed Matter*. Oxford University Press.

Joseph, P. & Tabeling, P. 2005 Direct measurement of the apparent slip length. *Phys. Rev.* E **71**, 035303(R).

King, M. R. & Leighton, D. T. 1997 Measurement of the inertial lift on a moving sphere in contact with a plane wall in a shear flow. *Phys. Fluids* **9**, 1248–1255.

Lauga, E. & Squires, T. M. 2005 Brownian motion near a partial-slip boundary: a local probe of the no-slip condition. *Phys. Fluids* **17**, 103102.

Li, H. & Yoda, M. 2008 Multilayer nano-particle image velocimetry (MnPIV) in microscale Poiseuille flows. *Meas. Sci. Technol.* **19**, 075402.

Lin, B., Yu, J. & Rice, S. A. 2000 Direct measurements of constrained Brownian motion of an isolated sphere between two walls. *Phys. Rev.* E **62**, 3909–3919.

Oberholzer, M. R., Wagner, N. J. & Lenhoff, A. M. 1997 Grand canonical Brownian dynamics simulation of colloidal adsorption. *J. Chem. Phys.* **107**, 9157–9167.

Oetama, R. J. & Walz, J. Y. 2006 Simultaneous investigation of sedimentation and diffusion of a single colloidal particle near an interface. *J. Chem. Phys.* **124**, 164713.

Peters, E. A. J. F. & Barenbrug, Th. M. A. O. M. 2002*a* Efficient Brownian dynamics simulation of particles near wall. I. Reflecting and absorbing walls. *Phys. Rev.* E **66**, 056701.

Peters, E. A. J. F. & Barenbrug, Th. M. A. O. M. 2002*b* Efficient Brownian dynamics simulation of particles near wall. II. Sticky walls. *Phys. Rev.* E **66**, 056702.

Pierres, A., Benoliel, A.-M., Zhu, C. & Bongrand, P. 2001 Diffusion of microspheres in shear flow near a wall: use to measure binding rates between attached molecules. *Biophys. J.* **81**, 25–42.

Pouya, S., Koochesfahani, M. M., Greytak, A. B., Bawendi, M. G. & Nocera, D. 2008 Experimental evidence of diffusion-induced bias in near-wall velocimetry using quantum dot measurements. *Exp. Fluids* **44**, 1035–1038.

Prieve, D. C. 1999 Measurement of colloidal forces with TIRM. *Adv. Colloid Interface Sci.* **82**, 93–125.

Sadr, R., Hohenegger, C., Li, H., Mucha, P. J. & Yoda, M. 2007 Diffusion-induced bias in near-wall velocimetry. *J. Fluid Mech.* **577**, 443–456.

Sadr, R., Li, H. & Yoda, M. 2005 Impact of hindered Brownian diffusion on the accuracy of particle-image velocimetry using evanescent-wave illumination. *Exp. Fluids* **38**, 90–98.

Santiago, J. G., Wereley, S. T., Meinhart, C. D., Beebe, D. J. & Adrian, R. J. 1998 A particle image velocimetry system for microfluidics. *Exp. Fluids* **25**, 316–319.

Sholl, D. S., Fenwick, M. K., Atman, E. & Prieve, D. C. 2000 Brownian dynamics simulation of the motion of a rigid sphere in a viscous fluid very near a wall. *J. Chem. Phys.* **113**, 9268–9278.

Unni, H. N. & Yang, C. 2005 Brownian dynamics simulation and experimental study of colloidal particle deposition in a microchannel flow. *J. Colloid Interface Sci.* **291**, 28–36.

Wereley, S. T. & Meinhart, C. D. 2005 Micron-resolution particle image velocimetry. In *Microscale Diagnostic Techniques* (ed. K. Breuer), pp. 51–112. Springer.

Xia, Y. & Whitesides, G. M. 1998 Soft lithography. *Annu. Rev. Mater. Sci.* **28**, 153–184.

Zettner, C. M. & Yoda, M. 2003 Particle velocity field measurements in a near-wall flow using evanescent wave illumination. *Exp. Fluids* **34**, 115–121.